The Astrophysical Journal, 816:103 (18pp), 2016 January 10 doi:10.3847/0004-637X/816/2/103

ON THE RETRIEVAL OF MESOSPHERIC WINDS ON MARS AND VENUS FROM GROUND-BASED OBSERVATIONS AT 10 μm

M. A. Lopez-Valverde[1], L. Montabone[2,4], M. Sornig[3], and G. Sonnabend[3,5]
[1] Instituto de Astrofisica de Andalucia, IAA/CSIC, Granada, Spain; valverde@iaa.es
[2] Space Science Institute, Boulder, CO, USA
[3] University of Cologne, KOSMA, Köln, Germany
Received 2014 December 17; accepted 2015 December 2; published 2016 January 14

ABSTRACT

A detailed analysis is presented of ground-based observations of atmospheric emissions on Mars and Venus under non-local thermodynamic equilibrium (non-LTE) conditions at high spectral resolution. Our first goal is to comprehend the difficulties behind the derivation of wind speeds from ground-based observations. A second goal is to set a framework to permit comparisons with other observations and with atmospheric models. A forward model including non-LTE radiative transfer is used to evaluate the information content within the telescopic beam, and is later convolved with the beam function and a typical wind field to discern the major contributions to the measured radiance, including limb and nadir views. The emission mostly arises from the non-LTE limb around altitudes of 75 km on Mars and 110 km on Venus. We propose a parameterization of the limb emission using few geophysical parameters which can be extended to other hypothetical CO_2 planetary atmospheres. The tropospheric or LTE component of the emission varies with the temperature and is important at low solar illumination but only for the emerging radiance, not for the wind determinations since these are derived from the Doppler shift at the non-LTE line cores. We evaluated the sources of uncertainty and found that the forward model errors amount to approximately 12% of the measured winds, which is normally smaller than the instrumental errors. We applied this study to revise a set of measurements extending for three Martian years and confirmed previous results suggesting winds that are too large simulated by current Martian circulation models at equatorial latitudes during solstice. We encourage new observational campaigns, particularly for the strong jet at mid–high latitudes on Mars, and propose general guidelines and recommendations for future observations.

Key words: methods: observational – planets and satellites: atmospheres – planets and satellites: terrestrial planets – radiation mechanisms: non-thermal – radiative transfer

1. INTRODUCTION

The characteristic strong CO_2 emissions at 10 μm in the upper atmospheres of Mars and Venus were originally detected about 40 years ago by ground-based observations using heterodyne spectroscopy (Betz et al. 1976; Johnson et al. 1976). They were explained as a population inversion following the strong solar absorption by CO_2 at 4.3 μm (Mumma et al. 1981; Deming & Mumma 1983). General-purpose non-LTE models for the CO_2 atmospheres of Mars and Venus can nowadays explain the observations and have been used to study their intensity (Lopez-Valverde & Lopez-Puertas 1994; Roldán et al. 2000), to estimate the altitude of the emission layer on both Mars and Venus, and to describe how it varies with parameters like the pointing altitude (in limb and nadir observations) and the solar zenith angle (SZA). Ground-based observations of these non-LTE emissions are becoming a routine tool to derive upper atmospheric parameters like wind and temperature on Mars and Venus. The winds in their mesospheres are obtained from the Doppler shift of the emission lines along the line of sight (LOS), while the kinetic temperature of the atmosphere is deduced from the rotational structure (Sonnabend et al. 2006, 2012).

However, ground-based observations at 10 μm still present challenges for their correct interpretation and application to remote sounding. On the one hand, and in addition to their non-LTE nature, one of the major complications is the large portion of the planet observed with the infrared telescopes used to date. Figure 1 shows an example from one of the campaigns described by Sonnabend et al. (2012) and devoted to deriving winds on Mars. It illustrates typical fields of view (FOV), or telescope-beam projections on the Martian disk. FOV between 0.8 and 1.6 arcsec are common, with the whole disk of Mars varying between 4 and 25 arcsec. Observations like these impose a large spatial averaging on the atmospheric properties to be measured and/or simulated. A significant modeling challenge is the need to address the extent to which each portion of the disk contributes to the emission, while simultaneously taking into account both nadir and limb geometries, the variations in optical thickness, and the non-LTE excitation of the rotational lines. Another difficulty associated with the beam size and the integration time of the observations is the variability of the mesospheric winds. As a result, the impact of such large averages on the interpretation of the measurements is difficult to estimate quantitatively without dedicated and precise radiative transfer modeling.

On the other hand, atmospheric global circulation models (GCM) for Mars, traditionally devoted to its lower atmosphere, extend nowadays to mesospheric and even higher altitudes (González-Galindo et al. 2009). Similar extensions in the case of Venus are also under development, triggered by new data from *Venus Express* (Lebonnois et al. 2008; Gilli et al. 2015). Although these theoretical frameworks compare satisfactorily with previous purely upper atmospheric models (González-Galindo et al. 2011), they do require data, particularly on

[4] Also affiliated to the Laboratoire de Météorologie Dynamique du CNRS, Université Pierre et Marie Curie, Paris, France.
[5] Present affiliation: RPG Radiometer Physics GmbH, Meckenheim, Germany.

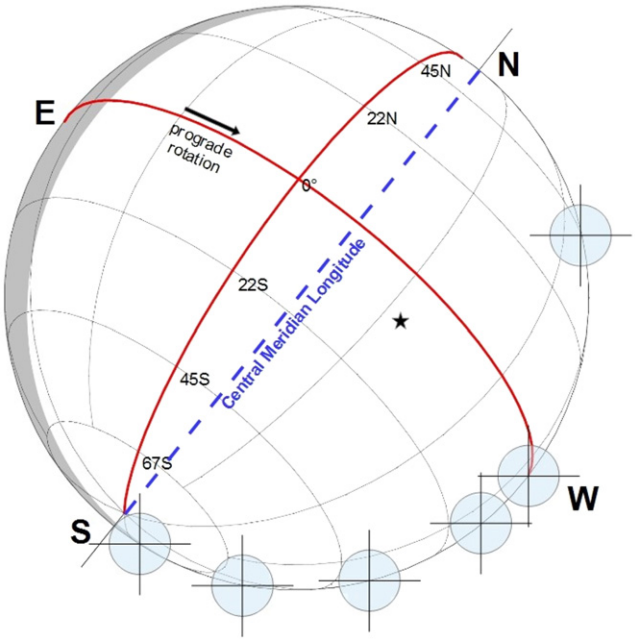

Figure 1. Example of an observational campaign for Mars with an almost complete illumination of the Martian disk (the star near the center indicates the subsolar point). Six different latitudes on the daylight limb are scanned, indicated by the small circles. Sky coordinates are used.

winds, to validate their predictions. Such data are scarce at mesospheric altitudes, and a comparison of GCM predictions of winds' speed and direction with ground-based observations is therefore very valuable. According to current GCMs, winds in the upper atmosphere of Mars are not only very variable in latitude, altitude, and time, but even their meteorological variability changes with season (González-Galindo et al. 2011). In principle, a rigorous comparison with data requires a careful extraction of the wind speeds in the 3D atmospheric region described by the precise radiative sounding mentioned above. This has never been done to date. Recently, Sonnabend et al. (2012) performed a comparison between their wind determinations on Mars from a series of three campaigns carried out between 2005 December and 2008 March (Mars years 27 and 28) and wind data extracted from the Mars Climate Database, or MCD for short (Millour et al. 2011, pp. 268–271; MCD version 4). However, they neither included a rigorous extraction of the winds nor considered all possible uncertainties. They recommended performing a detailed review of all the available (and future) measurements with a common well-understood method.

This work is the first part of an ongoing effort to design a sound strategy to compare ground-based measurements of mesospheric winds across different observations and with GCM simulations and to make recommendations to observers. It has three objectives. The first is to examine the steps of the calculation needed to correctly address this problem and to identify the uncertainties in typical observations. The second objective is to make a precise model to quantify the geometry, the radiative weighting functions, and their convolution with the beam functions, as well as to quantify the sources of error. The third, focused on Mars, is to apply this strategy to a set of previous measurements of Martian winds carried out during the last decade and to propose a set of general guidelines to future

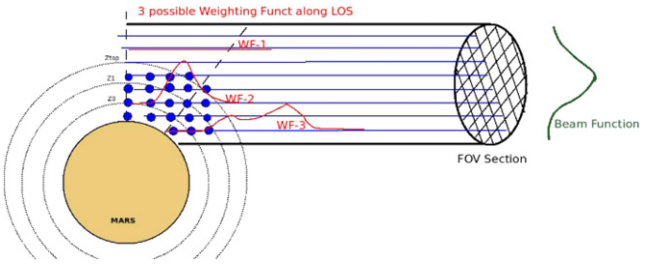

Figure 2. Schematic diagram of a telescopic beam pointing at a large area of the Martian disk, including limb and nadir ray-pointings. A number of blue points along different lines of sight illustrate the required discretization. The LOSs together with the "beam function" represent the 3D FOV and the geometry of the problem. Three weighting functions overplotted on three line of sights pointing at different tangent altitudes are added to illustrate that the radiative contributions vary with tangent altitude and with distance along the line of sight.

observers. A continuation of the present work will focus on Mars and specifically on an extensive validation of the MCD.

2. METHODOLOGY

The question of determining the wind field on Mars or Venus from telescopic observations is typical of an inverse problem with many more degrees of freedom than available observations, such that a unique solution does not exist. Still, it is worth knowing if there is a likely solution within the confines of a number of reasonable assumptions and understanding the meaning of such a solution, a task that requires a rigorous "direct forward modeling." In general, such a forward model can be expressed following Rodgers (2000) as

$$y = F(x) + \epsilon = F(u, b) + \epsilon \quad (1)$$

where the measurement y, the Doppler shift in our case, can be expressed as a functional form F of the atmospheric state x plus an error term ϵ. The forward model F contains the physics and geometry of the problem, including the winds u that we want to derive and other geophysical, instrumental, and modeling parameters b. The role of a precise forward model is essential to describe the emissions and their dependence on key parameters, in particular on the atmospheric wind field. This section is devoted to describing the formulation of such a forward model. Our strategy can be portrayed in five sequential steps.

Step 1. The first step was to define the geometry of the problem. The global picture is drawn schematically in Figure 2 for the case of Mars and helps to visualize the above-mentioned difficulties. We tried to plot as general a scenario as possible, so that it can be applied to any observation. Wind measurements are preferably performed by pointing the ground-based telescope at the edge of the planet's solid body. Such a limb observation gives the strongest signal in an optically thin medium like the upper atmosphere, since an atmospheric tangent path is much longer than a nadir one. However, as mentioned above, the nadir emission is also observed with current telescopic beam sizes. Two of the basic dimensions seen clearly in this plot are the "pointing altitude," z, in the vertical and the distance along the LOS, $x_{\rm LOS}$, in the horizontal. The beam cross section is shown as approximately circular in this sketch, and is best represented by the Airy function, A. This is associated with the instrumental characteristics and is assumed to be known at each point inside the circle. The width of the beam function requires an additional third dimension, α,

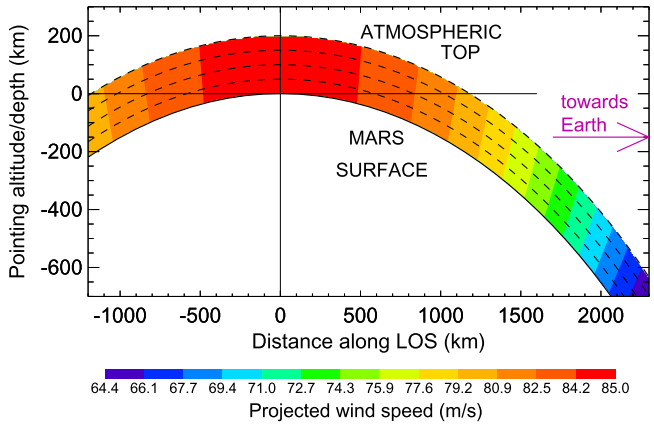

Figure 3. 2D cross section of the winds projected along the line of sight in our problem, for an idealized constant zonal wind of 85 m s^{-1}. As in Figure 2, the viewing direction coincides with the lines of sight and is indicated with the arrow "toward Earth." An atmospheric top at 200 km was used, and atmospheric layers at 50, 100, 150, 200 km are indicated with dashed lines. The shape of Mars looks distorted due to the focus on the vertical scale. The wind value is a maximum and equal to the zonal wind exactly at the limb (red area). See text for details.

to describe the problem accurately, i.e., $A = A(z, \alpha)$. In the figure we drew a few individual LOSs for several points in the beam. They extend to Mars' atmosphere, and collectively they might be seen as a longitudinal 2D cross section of the 3D beam. We also added a number of points along each LOS to indicate that a discretization is required; radiative transfer calculations need to be performed at these small steps along each LOS. This plot is used repeatedly throughout this work.

Step 2. Second, we used a radiative transfer model of the CO_2 emissions to define the emitting region in this 3D geometry, i.e., to determine which atmospheric layers contribute the most to the radiance measured from ground. This requires a computation of the radiative weights from all the altitudes sampled and throughout the 2D map of LOSs of the observations. Hereinafter we will refer to these weightings as the radiative contribution functions $C(z, x_{\rm LOS})$. They are defined in the Appendix. Given the non-LTE nature of the 10 μm emissions, these weightings are expected to vary significantly with SZA as well as with the optical thickness conditions. These changing conditions require a full non-LTE line-by-line radiative model and a sufficiently fine grid in (z, $x_{\rm LOS}$). For all these calculations we assumed an atmospheric reference state and a thermal structure appropriate to the observations. This is addressed in Section 3 below.

Step 3. A third question is related to the actual wind field in the atmosphere at each point of the grid, u. This is not known before the observations; on the contrary, it is the desired outcome. In this work, a wind field can be assumed as an input for the task of building the forward model. We started using a simple and idealized wind field for Mars, which consists of a horizontal/zonal component $u = 85$ m s^{-1} pointing toward the observer at the tangent point and at the center of the beam, with neither vertical nor meridional components.

Step 4. The only component of the wind field relevant to this study is that along the LOS, $u_{\rm LOS}$. The other two components neither can be determined from the data nor affect the observations. Hence, in a fourth step, the wind velocity vectors obtained at each point of the 3D grid required a geometrical projection in order to extract the LOS component. This is shown in Figure 3 for the simple wind field mentioned above. Two extreme cases are the limb and the nadir projections. Regarding the first, exactly on the limb the horizontal component includes the full modulus of the velocity vector. In our simplified wind field, all points near the limb are very close to the value of 85 m s^{-1}. Regarding the second, only a small fraction of the zonal wind is actually measured in this nadir part of the field of view. The absolute reduction in nadir can be very significant for strong winds and if the nadir portion of the beam is large. It decreases to a minimum of around 64 m s^{-1} in our example.

A "realistic" wind field can be built using the values provided by wind climatologies appropriate to the time and location of the observations, as done by Sonnabend et al. (2012) with the Mars Climate Database. The MCD is particularly well-suited to the 3D interpolation exercise mentioned above, as it incorporates a routine to extract the fields at arbitrary points within the limits of the database. In fact our study can be used to validate such a database, by permitting a data-model comparison. Such an application of this study is an ongoing effort.

Step 5. The final task was to combine the radiative weighting functions with the projected winds and with the Airy function to simulate the total emission and the averaged Doppler shift. This is discussed in Section 4 below. The value obtained after this step would include all the physics and the geometrical issues, and should be representative of the wind field assumed, or could be compared to the observed values.

Let us recall at this point a few assumptions used in this strategy. A very basic one is that the radiative and geometrical weightings to be described in the following sections do apply both to the radiance level observed and to the wind velocities to be derived. The rationale for this follows from the linear relation between the Doppler shift and the wind speed, $d\lambda/\lambda = u/c$. Insofar as λ does not change significantly, and it does not within the width of a rotational line, the averaging of the velocities, and that of the Doppler shifts $d\lambda$, will follow the superposition of information given by the radiative weightings to the total emission.

As a result, both the emission and the wind to be measured can be seen as averages or triple integrals over the three dimensions of the problem (z, $x_{\rm LOS}$, α):

$$\hat{R} = \int_z \int_\alpha \int_{x_{\rm LOS}} C(z, x_{\rm LOS}, \alpha) A(z, \alpha)\, dx_{\rm LOS}\, d\alpha dz \qquad (2)$$

$$\hat{u} = \frac{\int_z \int_\alpha \int_{x_{\rm los}}^{\rm MESO} u_{\rm los}(z, x_{\rm los}, \alpha) C(z, x_{\rm los}, \alpha) A(z, \alpha)\, dx_{\rm los}\, d\alpha dz}{\int_z \int_\alpha \int_{x_{\rm los}}^{\rm MESO} C(z, x_{\rm los}, \alpha) A(z, \alpha)\, dx_{\rm los}\, d\alpha dz} \qquad (3)$$

where a normalization term was included in the wind expression. As explained in the Appendix, this normalization term is not the measured radiance, $\hat{R}$ in Equation (2), because of an important difference between Equations (2) and (3) regarding the extent of the integral along the LOS. The wind expression has to be evaluated only throughout the mesospheric portion of the LOS. The reason is that the Doppler shift is evaluated only from the spectral shift of the core of the emission lines observed, and these come from the mesosphere. The broad absorption feature outside the line core, i.e., the

radiance originated at lower altitudes (in the troposphere) is irrelevant during such fitting of the line core. Let us recall that the emission line cores from mesospheric altitudes are very narrow, in comparison with purely absorption lines (Lellouch et al. 2008). Equation (3) is formally equivalent to Equation (1), where the Doppler shift y has been replaced by the measured wind u and the error term has been ignored. The rest of the physical and geometrical parameters b of the forward model, in Equation (1), are contained in the radiative term C and in A, i.e., in the simulation of the mesospheric radiances.

A second caution relates to the complication of computing radiative contributions under different Doppler shifts along the LOS. If very different $u_{\rm LOS}$ were found along the LOS, the atmospheric emission would be Doppler shifted by different amounts along the LOS, and consequently, different wavelengths would contribute to the overall emission. In principle the radiative contributions C, which are wavelength-dependent, would need to take this into account before their combination with the beam size. In practice, however, using Mars as an example and considering a value of 50 m s^{-1} as a moderate to strong Martian mesospheric wind, differences in wind speed of that order represent Doppler shifts of 0.00017 cm^{-1}, a tenth of a typical half width in the mesosphere of Mars (López-Valverde et al. 2011). Therefore, this is a very small effect and was ignored in our calculations, which are devoted to the center of a strong CO_2 spectral line (P4, at 957.8 cm^{-1}) of the 10 μm band. The winds observed do correspond to averages along the LOS and can be correctly represented with the C functions at the line core.

A third remark, somewhat related to the previous one, is that we focus here on the line core only. The heterodyne observations we are analyzing in this work have a very good spectral resolution and normally contain several lines of the 10 μm band, and this minimizes the fitting uncertainty. The short frequency range around the line core required for the fitting, and the absence of asymmetries in the observed emission lines, guarantee that the fraction of the line shape used in the fitting process is small. Consequently, all its wavelengths are sampling the same altitude range, and we expect the fitting process to be well defined by ignoring distant wavelengths and tropospheric absorption features. We assume the observers take the caution to evaluate their fitting error. This error component will be included later in our analysis (Section 6).

In the following sections we will discuss both the total radiance observed (tropospheric + mesospheric) and the mesospheric-only component (the only relevant contribution for wind determinations), as both are related and their study helps in understanding the observed winds.

3. NON-LTE RADIATIVE TRANSFER CALCULATIONS

Our simulations of the 10 μm emission in the Martian and Venusian mesospheres are performed with a line-by-line radiative transfer code that handles nadir and limb geometries and non-LTE populations. We focus here on the case of Mars, without lack of generality, and will discuss below some differences with Venus.

Before the calculations are performed, a certain atmospheric reference state needs to be assumed. In the case of Mars this was extracted from the MCD for the conditions: latitude 33° N, longitude 125° E, local time (LT) = 15.7, SZA = 60°, which

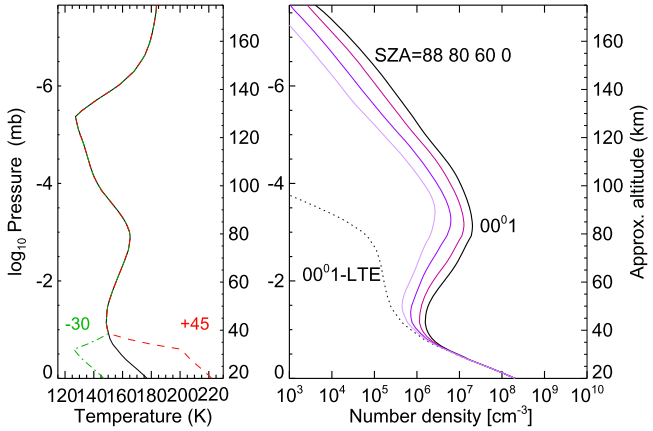

Figure 4. Right panel: vertical profile of the (001) state populations during daytime for several SZA values, as indicated. The LTE population (much smaller) is shown for comparison. Left panel: thermal profile used in the calculations and two modifications of +45 K and −30 K below 40 km.

correspond to one of the observations reported by Sonnabend et al. (2012) (see their Campaign C, Table 3). The vertical temperature profile is shown in Figure 4, left panel. The calculations were carried out in a sufficiently fine grid, with 4 km steps in the vertical and 10 km steps in the horizontal (along the LOS). This was done for all tangent altitudes from −700 km (700 km below the surface, i.e., nadir pointing) up to 200 km above the ground (i.e., limb sounding).

The first step is to compute the non-LTE populations. These are obtained with the generic non-LTE model of López-Valverde et al. (2011). These authors studied vibrational temperatures of the CO_2 upper level (00^01) and lower levels (02^01 and 10^00) of the 10 μm bands. The emissions in the model are produced by solar pumping, mostly in the strong 4.3 μm fundamental band of the (00^01) state, followed by radiative relaxation in the optically thinner 10 μm bands to the lower states. There are other collisional and radiative de-excitations of the (00^01) state, as well as other excitation processes of the upper state included in the model. For full details the reader can also see Lopez-Valverde & Lopez-Puertas (1994). One of the largest uncertainties is the collisional exchange of vibrational excitation between some excited states. This effect is relevant for CO_2 states at higher energies than the (001) level. In addition, it is systematic and approximately similar for all SZA, and therefore would not affect the SZA discussion here.

Instead of vibrational temperatures, Figure 4 directly shows profiles of the non-LTE populations of the (00^01) state of the main CO_2 isotope for several SZA values. There is a clear enhancement around 80 km which produces the peak radiance at that altitude, as previously obtained by López-Valverde et al. (2011). The altitude or pressure level of this peak emission hardly varies with SZA, but the number of excited molecules does, and it decreases strongly when the solar pumping fades. This effect is relatively small within low SZA values (below 60°). It can also be seen that below 40 km, when LTE prevails, SZA has negligible effects, and daytime and nighttime results coincide. The altitude range that actually contributes to an emission line is between 50 and 110 km, as we will see below.

The CO_2(001) state populations can be used to compute the contribution functions along the LOS, $C(z, x_{\rm LOS})$. The results, for the specific rotational line P4 and for our nominal atmospheric state, are shown in Figures 5 and 6. Figure 5

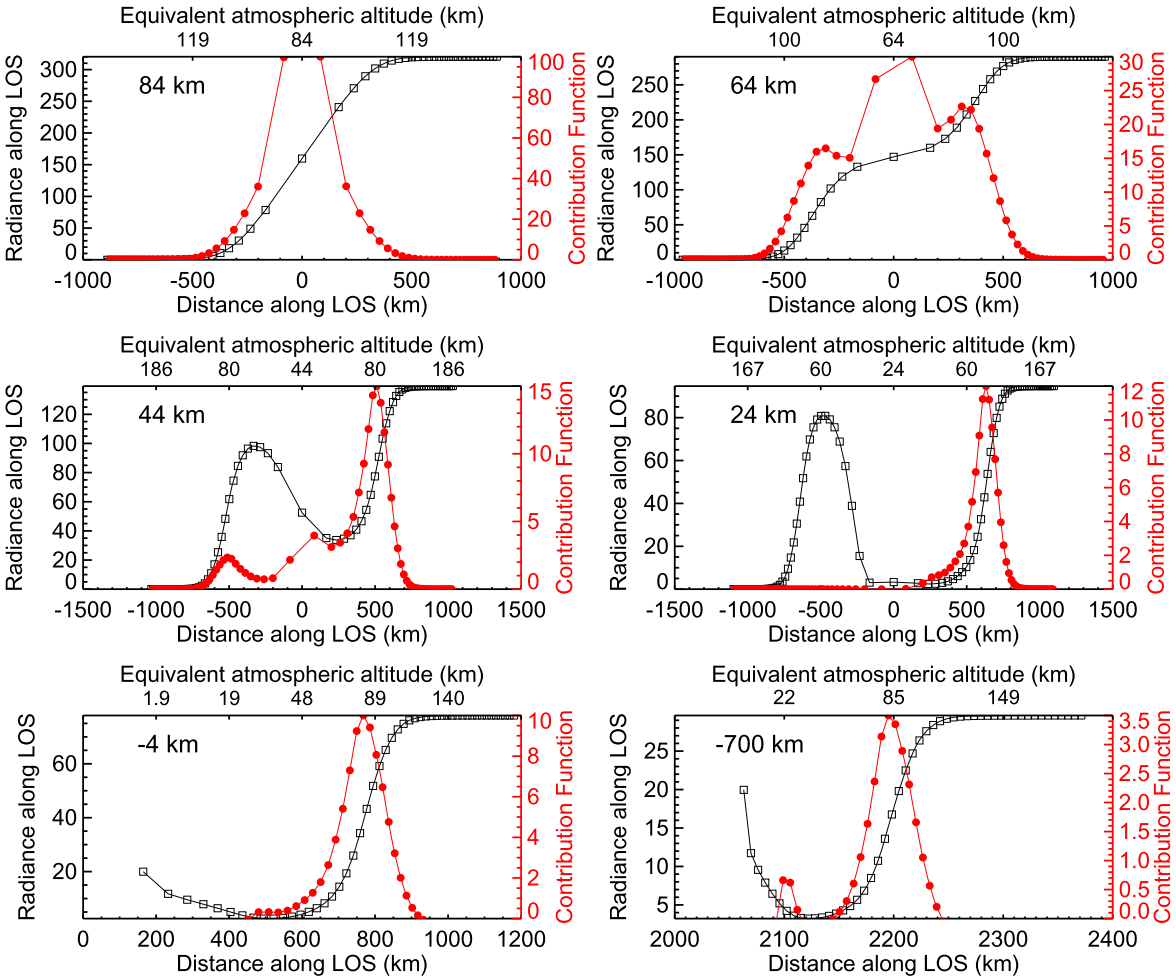

Figure 5. Radiance seen by an observer moving along the LOS (black lines) and contribution functions (red lines) along the LOS, at six tangent altitudes, pointing from 84 down to −700 km. The *X*-axis is distance along the LOS, as in Figure 3, with origin at the edge of the solid planet. The corresponding altitude in the atmosphere is shown on the top *X*-axis. The Earth (observer) is at infinity to right of the plot, as in Figure 3. Radiance units: erg s^{-1} cm^{-2} sr^{-1} cm^{-1}. Contribution function units: erg s^{-1} cm^{-3} sr^{-1} cm^{-1}.

plots C for four different tangent altitudes in the limb, $z = 84$, 64, 44, 24 km, and for two nadir-looking views, $z = -4$, −700 km. The figure also shows the radiance $R^{\rm OBS}(x_{\rm LOS})$ that an observer would see when looking at Mars as he moves along the LOS toward Earth (see the Appendix for details). Figure 6, left panel, shows all the contribution functions (for all the pointing altitudes) in a 2D cross section of the beam (like a cut through the axis of the beam). Its right panel shows the profile of the total emission, $R_{\rm LOS}(z)$, at every pointing altitude z, i.e., the integration of the contributions $C(z, x_{\rm LOS})$ along the LOS.

Lets us focus first on Figure 5, specifically on its upper-left panel, which points to the limb at 84 km above the planet. As in Figure 3, the Earth observer is to the right-hand side. At the farthest end of the LOS from the observer's viewpoint (to the extreme left-hand side, or $x_{\rm LOS} = -\infty$) the atmospheric emission is essentially zero. Notice that $x_{\rm LOS}$ is transformed into actual atmospheric altitude on the upper *X*-axis. The radiation increases as the observer moves to the right, and is exactly half the total emission at the center of the LOS ($x_{\rm LOS} = 0$ km at the tangent point; the atmospheric altitude is 84 km there). This is the common behavior under optically thin conditions, typical of layers at very high altitude. The center of the P4 line is optically thin everywhere along the LOS, and therefore its contribution is proportional to the length of the path. This is largest exactly at the tangent point $x_{\rm LOS} = 0$ km. As a consequence, the contribution function has a Gaussian or "Chapman layer" shape.

At 64 km, just below the peak of the non-LTE excitation region, the situation has changed a little bit. The strongest lines of the 10 μm band start to be optically thick for limb ray-tracings. In the center of the LOS, the optically thickest segment of the LOS, CO_2 absorbs some of the 10 μm photons coming from layers farthest away from the Earth's observer. The radiance seen by an observer moving along the LOS toward Earth presents two strong increases, which occur when crossing the peak non-LTE emission layers around 80 km, and it decreases at the actual tangent point. The contribution function has therefore two lobules around 80 km. It also presents an additional contribution in the center of the LOS for geometrical reasons (the longest paths are there). Notice that the lobule at 80 km on the left gives a smaller contribution than that on the right. This is because of the absorption of the farthest non-LTE emission layer that takes place in the center of the LOS.

At pointings of 44 km, much lower than the peak non-LTE excitation layer, the central part of the path has become very optically thick in the core of this 10 μm line, absorbing much of the radiance emitted in the farthest hemisphere. For the

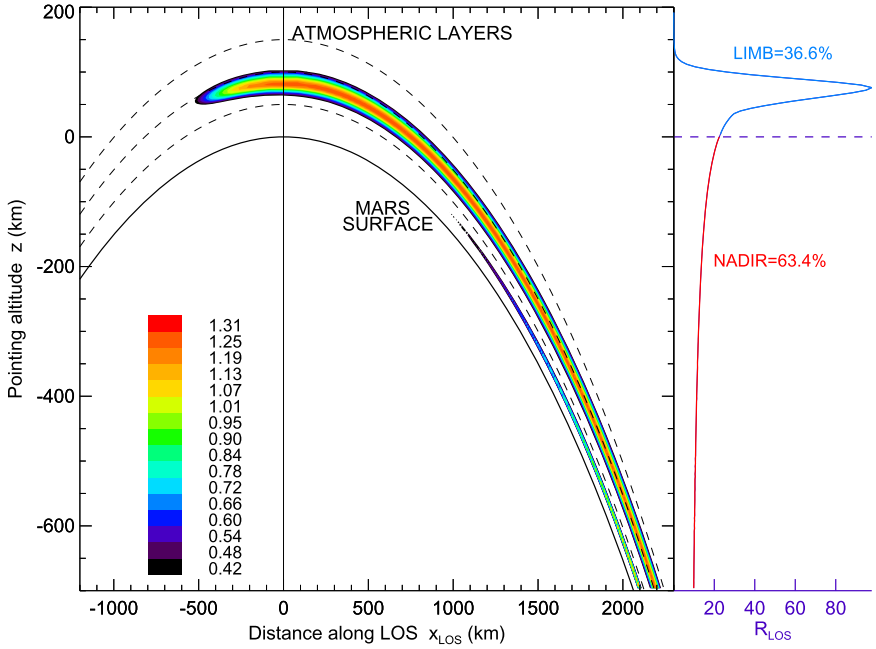

Figure 6. Left panel: simulation of the non-LTE 10 μm emission layer in a 2D cross section of Mars' atmosphere as described by the contribution functions along horizontal LOSs from an observed to the right of the figure, in a geometry entirely similar to Figures 3 and 5. Right panel: emerging radiance at each tangent altitude (integrated contributions along the LOS), separating nadir and limb ray-tracings. Calculations are for SZA = 60° and the thermal structure of Figure 4. Radiance units are as in Figure 5.

pointing at 24 km, such an absorption is almost complete. At this low pointing, even the central emission around the tangent point (geometrically enhanced emission) has a very small contribution. Two emitting lobules are seen in the black curve, located at the non-LTE layers, but only that on the right-hand hemisphere (closer to Earth) can be detected. This is good news with respect to the sounding of the Martian mesosphere at 10 μm, because the emission essentially comes from a well-defined region around 85 km, where the non-LTE emission peaks.

During nadir sounding (two lower panels in Figure 5) the shape of the weighting functions is similar to the 24 km limb case, especially when the pointing is close to the limb. At −4 km we see that both the emission from the surface (20 radiance units) and that from the lowest atmospheric layers are greatly absorbed below about 20–25 km, and only the strong non-LTE emission around 75 km and above can escape to space and give a significant contribution. Therefore, in nadir the non-LTE peak region, located around 80 km, is also an important contribution to the total emission. Further, we can see clearly that the emission line originates at altitudes above about 50 km in both limb and nadir viewings. This is an encouraging result regarding nadir and limb similarities. However, when pointing at 700 km below the surface, a small emission from a layer around 22 km appeared that is either not present or much smaller in the limb. The reason is that the optical thickness in a purely nadir view is much lower and the emission from the troposphere (in LTE) can give a significant contribution. Although small in this particular calculation, we will see below that this effect is more important at high SZA, when the non-LTE excitation declines. This would be an undesirable effect if our goal was the separation of tropospheric and mesospheric components in the observed/emerging radiance. However, since the goal is to measure the Doppler shift we can ignore the tropospheric contribution, as mentioned above.

These results confirm the assumption in previous work that the derived winds correspond to the mesosphere. Sonnabend et al. (2012) acknowledged that the winds are retrieved in a broader region, centered on the atmospheric peak emission at 10 μm as given by López-Valverde et al. (2011). But they mentioned a possible contribution from the troposphere that is difficult to estimate. In this work we present a methodology (or forward model) to describe precisely the limb-brightening of the mesosphere and all the related uncertainties.

Figure 6, left panel, puts together all the contribution functions for both nadir and limb calculations in a global view. As explained above, both limb and nadir have a strong peak at mesospheric altitudes, near the location of the non-LTE excitation. Notice also that the emission value in the center of the mesospheric peak is similar at all locations. This is because the non-LTE emission is mostly dependent on the SZA, and when this is fixed the emission is also constant. Notice the small contribution from tropospheric altitudes in the nadir portion of the plot.

The right panel shows the profile $R_{\rm LOS}(z)$, which reveals clearly the geometry of the problem. The limb portion, although much thinner than the nadir in extent, represents a very significant fraction of the total radiance observed. In this particular case, for the assumed reference atmosphere and SZA, and with a beam size and pointing extending to 700 km below the surface of Mars, the limb is responsible for nearly 40% of the emission. Hereinafter we will refer to this situation as the non-LTE atmospheric limb-brightening of the planet and we will study below the dependence of the $R_{\rm LOS}$ profile on various geophysical parameters.

4. PROJECTION AND CONVOLUTION WITH BEAM FUNCTION

As mentioned above (Equation (3)), once the winds are projected along the LOS, and the radiative weightings are known, both need to be convolved with the beam's Airy

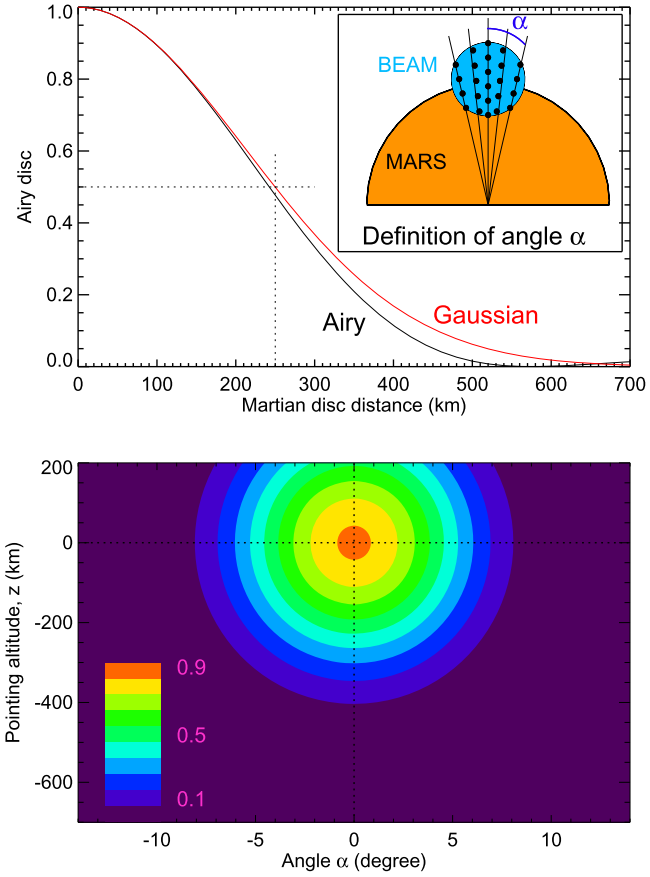

Figure 7. Airy disk typical of a ground observation campaign (after Sonnabend et al. 2012). The pointing altitudes in the bottom panel correspond to the same range as in Figure 6, and the center of the beam is assumed to point to Mars' surface (zero altitude). The top panel shows a 1D profile from the center of the disk together with a Gaussian approximation (see text). The angle α, defined in the inset of the top panel, refers to the center of the beam. For each angle or "ray" a series of dots indicate that a vertical discretization is used (steps given by the radiative transfer study). See text for details.

function to obtain a wind averaged with the emission in the whole FOV.

Figure 7 shows a typical Airy function and the geometry used to characterize it. Following Sonnabend et al. (2012), we use a simple Gaussian centered in the beam FOV, which is assumed to point to the edge of the Martian disk ($z = 0$ km). We used the angle α, defined unambiguously from the center of Mars. Again, a discretization is required to perform the integration throughout the beam. In this study we used small angular steps around the center of the beam. For each value of α, several points in the vertical were used, defined according to the vertical resolution in the radiative transfer calculations (4 km). Typical angular sizes of the beam core are equivalent to 10°–15° in latitude. Our angular step was 1°; negligible changes in the calculations were obtained for smaller values. One may notice that the Gaussian function fits the Airy disk very well in the central part, but then deviates away from it. The error in the area in our case is about 7%, but the strong limb emission is close to the center of the beam, where the error in the Gaussian is smaller. For this reason, typical errors in the area of the product Airy $\times$ $R_{\rm LOS}$ are <4%. However, if the beam is shifted by about 250 km, the Gaussian error (in the area of the curve) reaches ~8%.

Figure 8 shows an intermediate step in the wind convolution mentioned above: here only the radiative contributions and the beam function are convolved, while Figure 9 in addition incorporates the wind field. In precise terms, Figure 8 shows the integral's kernel of the denominator of Equation (3) on a (z, α) map, while Figure 9 shows the variation with pointing altitude z of the integral's kernel of the numerator of Equation (3) for $\alpha = 0$.

In both figures, three positions of the beam were used with central pointings at the surface of Mars, at 250 km above, and at 250 km below. This vertical shift is used to study the impact of possible telescope pointing/alignment uncertainties, and represents about a third of our FOV. Let us recall that this is the diffraction-limited FOV. Uncertainties from seeing conditions and unwanted telescope movements would be equivalent to larger pointing errors. Comparing the right panel of Figure 7 and the central panel of Figure 8, one can appreciate the effect of the radiative weightings. The combination of both $R_{\rm LOS}(z)$ and $A(z, \alpha)$ forms a well-defined region within the beam, which contains the maximum information gathered. This has a clear peak in the limb portion of the FOV, close to the peak non-LTE excitation. There is also some contribution from the nadir portion closest to the limb–nadir transition ($z = 0$). The nadir component decreases away from this point because both the radiative contribution and the Airy function decrease. The combined function is symmetrical around the center of the beam because the beam function is symmetrical and because, for simplicity, in this calculation the radiative contribution was assumed to be constant with α.

When this function is convolved with the winds, one obtains the green curve in Figure 9. This curve has a strong peak in the mesosphere, in the center of the maximum sensitivity region, and shows some contribution from nadir, as mentioned above. The resulting wind has a value around 82 m s^{-1}, about 3% lower than the constant wind of 85 m s^{-1} assumed at the tangent point. This value could be an estimation of the error in this idealized wind field if one assumes that the wind measured from ground comes from one single location. We will see below that this error can be significantly larger depending on SZA, the tropospheric conditions, and the wind field itself.

A shift of the beam position downwards from the "nominal" pointing by 250 km deforms the shape of the "maximum information" region (MaxInf, hereinafter) to that observed in the right panel in Figure 8, and to the red curve in Figure 9. The relative weight of the nadir contributions increased, and the resulting wind is reduced to 78.5 m s^{-1}, about 8% lower than the maximum at the tangent point. Similarly, the upwards shift of the beam reduces the nadir contribution significantly (left panel in Figure 8). Almost all the information now comes from the limb, and the resulting global average wind is 83.6 m s^{-1} (blue line in Figure 9), just 1.6% lower than the tangent nominal wind. If a 250 km shift in the beam pointing is considered as a typical value of the uncertainty in regular observations, our calculations suggest that the error associated in the wind may be about 6%, which is the difference between our calculations in the two extremes. But again, this value surely varies with parameters that affect the limb/nadir partitioning and with the wind field itself.

In addition to the pointing uncertainty in the "vertical," there will also be an uncertainty in the "horizontal" direction, i.e., along the surface of the planet, or the actual latitude of the beam. In principle this does not alter the previous discussion;

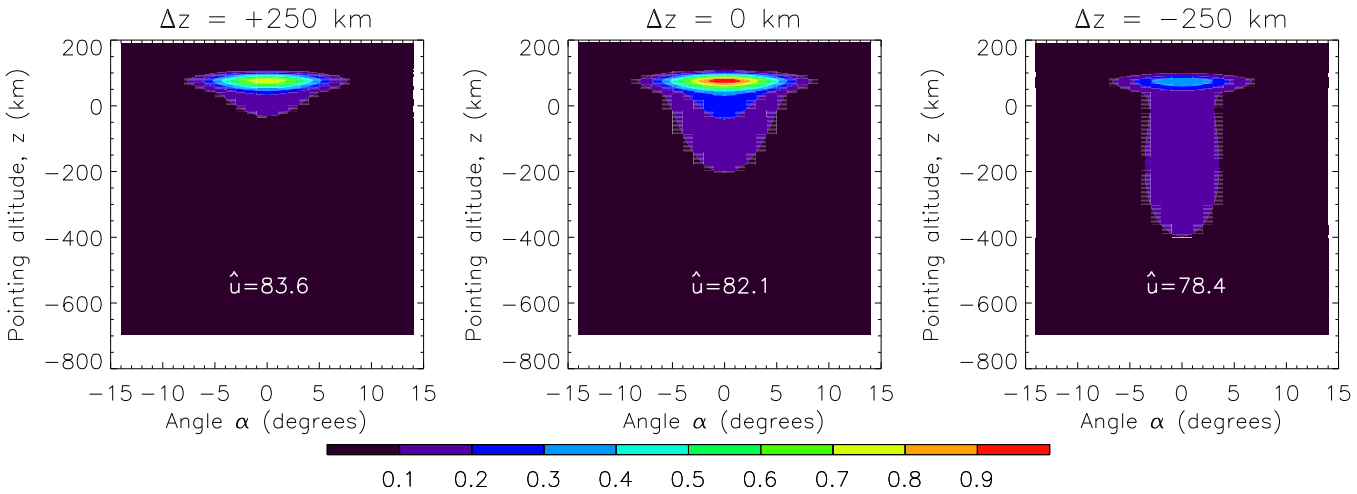

Figure 8. 2D map of the radiative and Airy-disk weightings as a function of α and pointing altitude z (see text). The function is normalized to [0, 1], computed for SZA = 60°, and shown for three vertical shifts in pointing: 250 km upwards (top panel), no shift (nominal results, central panel), and 250 km downwards (toward the center of Mars; bottom panel). The winds obtained after all averages and normalization are 83.6, 82.1, and 78.4 m s^{-1}, respectively.

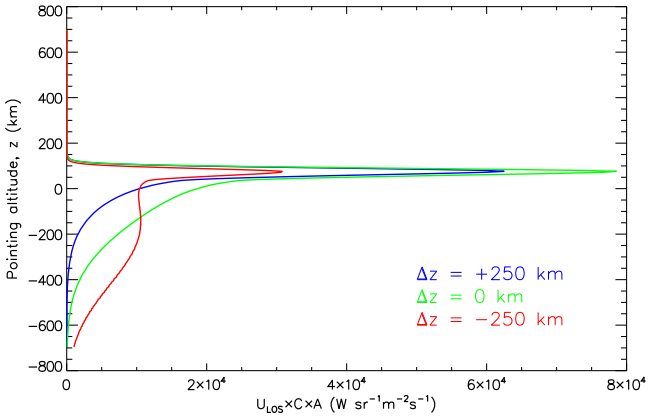

Figure 9. Vertical profiles of the averaged winds along each LOS including the radiative contribution functions and the Airy-disk function, for the three pointings $z = 0$, $+250$, -250 km, as indicated. Calculations are for SZA = 60°.

the weightings and the resultant shape of the "maximum information region" will just move by some degrees in latitude. Also, if the SZA changes significantly across the FOV, it may alter the symmetry of the MaxInf region. But these are considered effects of secondary importance.

5. SENSITIVITY STUDIES

The non-LTE emission at a given altitude is expected to vary with diverse geophysical parameters, mostly with the atmospheric density (or altitude) as shown above in Figures 4 and 6, and with the SZA.

Non-LTE parameters may also play a role in the intensity of the non-LTE emission. Among them, collisional rates of the fast vibrational–vibrational exchanges during molecular collisions are uncertain to a high degree, particularly in collisions involving isotopic and high-energy states. Their impact on the vibrational temperatures was discussed by López-Valverde et al. (2011). But these rates would introduce systematic changes common to all SZA and mesospheric altitudes, and will hardly change the shape of the radiative contributions. Therefore their impact on this study is minimal, and we do not consider them further here.

We focus next on two important variables, the temperature and the solar illumination. As we will see below, there is a link between them, but we discuss them here separately for the sake of clarity. We will discuss their impacts both on the total radiance and on the mesospheric-only emission, i.e., on the measured winds.

5.1. Atmospheric Thermal Structure

Once more we need to separate here the LTE and the non-LTE regions, with a transition around 50 km in the case of Mars (which for our purposes can also be considered as the troposphere-to-mesosphere transition). Temperature plays different roles in each of these regions. The equivalent transition layer on Venus would be located at around 90 km, and will be used here as the separation between a lower and an upper mesosphere. In this work, for most of our discussions the Martian troposphere (0–50 km) and the Venus lower mesosphere (60–90 km) are equivalent.

Starting with the tropospheric or LTE region, and according to Figure 6, this gives a significant contribution to $R_{\rm LOS}$ only in the nadir portion of the FOV. The emission actually comes from a well-defined layer around 20–25 km altitude (about 0.4 mbar). The relevant parameter is therefore the temperature at this pressure level. Its importance for the total radiance, compared to the mesospheric component, will depend also on the magnitude of the non-LTE mesospheric emission, and therefore on the SZA. Under strong solar illumination (SZA $< 60°$), unless the troposphere is extremely warm, it will give a small contribution compared to the non-LTE component. However, at high SZA the troposphere may become significant (in relative terms, because the mesospheric component decreases). This is illustrated in Figure 10, which shows contribution functions in the limb and in nadir, similar to Figure 5 but for a set of four SZAs. The contribution functions have been normalized to their LOS-integrated value $R_{\rm LOS}$; in other words, all curves have the same area. This normalization highlights the shape of the function and its relation to the SZA. At high SZA, the nadir component shows two maxima, one from the troposphere, in LTE, and another from the mesosphere, in non-LTE. Even for limb pointings below the peak

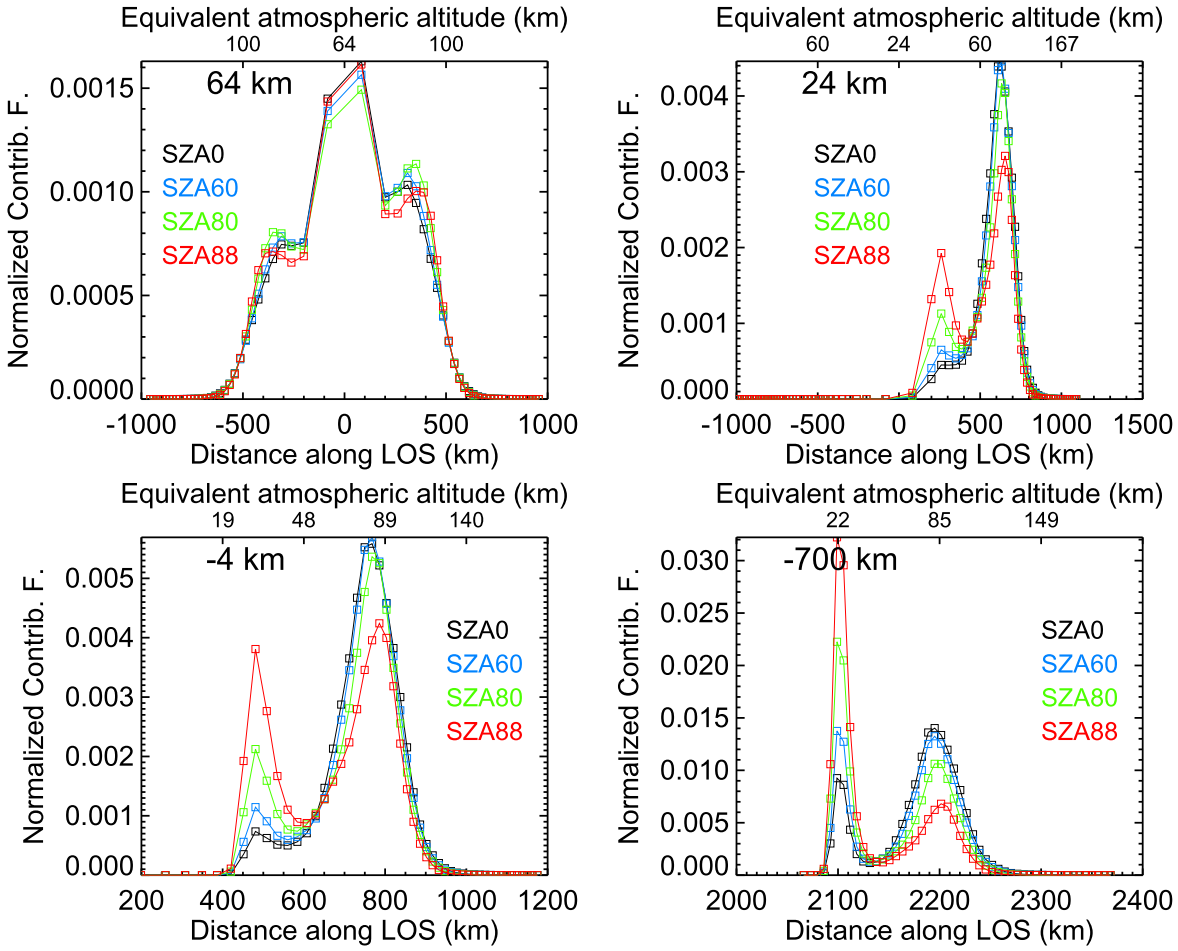

Figure 10. Contribution functions $C(z, x_{\rm LOS})$ at 10 μm along the LOS for tangent altitudes $z = -4$, -700 km in nadir and $z = 64$, 24 km in the limb, and for different values of SZA, as indicated. Contribution function units as in Figure 5 but here they are normalized to their total, integrated value $R_{\rm LOS}$ (see text).

non-LTE region (panel at 24 km tangent height) the tropospheric component can be significant at high SZA.

Let us focus now on the temperature effects on the non-LTE region. Here, the population of the emitting state is largely independent of the local kinetic temperature. The thermal structure has only an indirect significance, which is mostly due to the variation of the altitude–density profile via hydrostatics. The basic effect of a very warm lower atmosphere would be to raise the altitude of the peak absorption, but the pressure level of the emission peak would be the same. The profile of contribution functions shown in Figure 6, and consequently the peak in Figure 9, would simply be shifted upwards by the same amount.

A few recent studies have evaluated the impact of the Martian lower atmosphere on the vertical shift of a given layer. One of them is the 4.3 μm peak emission observed by OMEGA (Piccialli et al. 2011); another is the analysis of the altitude of the peak electron concentration (González-Galindo et al. 2013). These studies suggest that seasonal and local time variations in the 10 μm peak emission might be as large as 10 km at the equator; this is a small shift compared with other uncertainties such as the beam pointing mentioned above.

In order to test the constancy of the pressure level of the emission peak under extreme changes in the thermal structure of the atmosphere, we can compare with calculations for the atmosphere of Venus. For Venus we assumed the daytime VIRA reference model (Hedin et al. 1983; Seiff et al. 1985), and the same set of SZA: 0°, 60°, 80°, and 88°. The results showed similar conclusions to the Martian case: a non-LTE limb-brightening and smaller emissions in the nadir portion of the FOV. The Venusian peak emission was found around 108 km altitude, or 2.5×10^{-3} mbar, a value close to the Martian pressure at about 75 km altitude (1.2×10^{-3} mbar).

In conclusion, any observational strategy intended to measure the total emission (troposphere and mesosphere) needs to carefully consider the effects of the lower atmospheric thermal structure. In principle, the colder the troposphere the better, because the total emission will be more confined to the limb portion, where the emission layer is very well defined. High SZA should also be avoided for this reason. However, for wind measurements, only the indirect effect due to hydrostatics is significant and it is of little concern.

5.2. *Effects of Solar Illumination*

The SZA is a key parameter in non-LTE phenomena like the present case of solar fluorescence, and Figure 4 above shows the significant effect of this parameter on the vibrational populations of the emitting state.

Figure 11 illustrates the SZA effect on the $R_{\rm LOS}$ profiles for Mars and Venus. The left panels show the calculated $R_{\rm LOS}$ without any normalization, similarly to Figure 6, while the panels on the right compare the $R_{\rm LOS}$ shapes, i.e., normalized to their peak values. First, the figure shows as expected that the

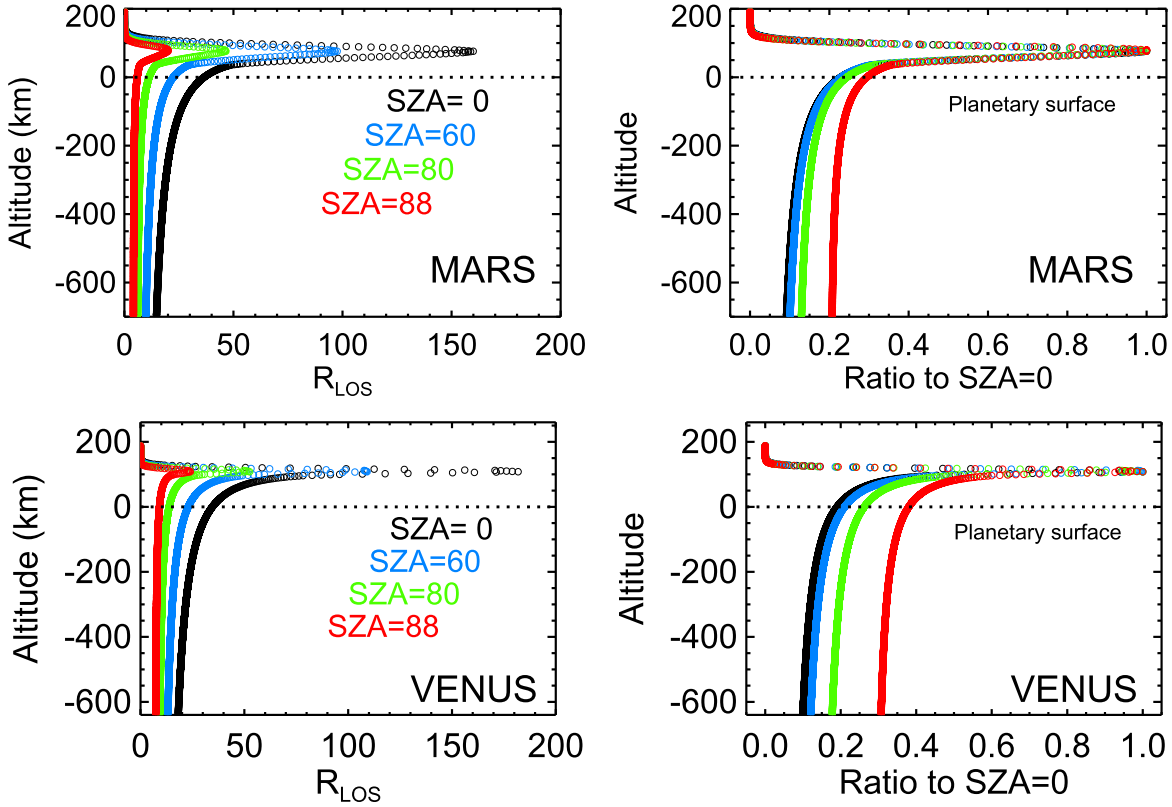

Figure 11. Left panels: LOS radiance profiles at SZA = 0°, 60°, 80°, 88° for Mars (upper panels) and Venus (lower panels). Radiance units as in Figure 5. Right panels: the same profiles but normalized to their peak emission. See text.

emission is largest at the subsolar point, SZA = 0°, and decreases strongly toward the terminator (SZA = 88°). As a consequence, we suggest carrying out observations at positions in the Martian disk with a significant solar illumination. Notice also that the non-LTE peak layer on Venus is much narrower in its vertical extent than that on Mars. This is a result of the lower scale height on Venus, essentially due to its larger gravity. Second, the ratio-ed $R_{\rm LOS}$ in the right panels show that the vertical profiles have a similar shape for all the SZA, but the nadir component is largest at high SZA. As mentioned above, this result reflects the larger relative contribution of the tropospheric component when the non-LTE emission decreases.

To better evaluate this tropospheric contribution to the emerging radiance, Figure 12 (top-left panel) shows calculations of the $R_{\rm LOS}$ profile for nighttime conditions for the Martian thermal profile used in this work and for two modifications (of −30 K and +45 K) around this profile at tropospheric altitudes. The three profiles are shown in the left panel of Figure 4. In contrast to the daytime limb-brightening, in the absence of the mesospheric non-LTE component the $R_{\rm LOS}$ profile shows a completely different behavior. It has a very small limb component, which decreases rapidly with altitude, as does the atmospheric density. Also the nadir component decreases toward the edge of the planet, as the optical thickness moves the actual emission layer to higher altitudes, where the temperature is lower. The decrease of the atmospheric density and temperature with altitude and the LTE assumption produce this limb-darkening shape. Varying the tropospheric temperature will alter the emission levels but not this overall behavior. We observe a difference of a factor 6 in the emission at the deepest point (−700 km) between our two extreme tropospheric temperatures, −30 K and +45 K. The difference between the blackbody emissions of the two profiles around 25 km (the altitude of the effective emission) is much larger. However, the 25 km value was obtained for the nominal thermal structure. The atmospheric transmittance normally increases with temperature and, vice versa, a colder atmosphere is optically thinner. The result is that the actual emission altitude occurs around 10 km in the coldest profile and around 30 km in the warmer case, and the comparison of the blackbody temperatures at those altitudes does explain that factor 6 difference. The particular perturbation values of −30 and +45 K were chosen with the intention of covering wide thermal variations and to illustrate quantitatively the impact of unknown tropospheric conditions on the emerging emission profile. Notice that the convolution with the beam function will reduce the nadir region that actually contributes to the measured radiance. The three dashed lines in the top-left panel of Figure 12 indicate this effect. Unless the troposphere is very warm, the uncertainty comes from a broad region but much less than the whole beam.

A relevant result for Doppler measurements of wind is obtained when the LTE or nighttime contributions are subtracted from the daytime results. This is equivalent to removing the tropospheric component and leaving the mesospheric non-LTE emission alone. The obtained profiles, which we can denote $R_{\rm LOS}^{\rm MESO}$, are shown in the top-right panel of Figure 12. Another difference between this panel and Figure 11 is the extension of the study to three additional SZA values. By removing the tropospheric contribution the nadir component shows exactly the same SZA variation as in the limb. And if we

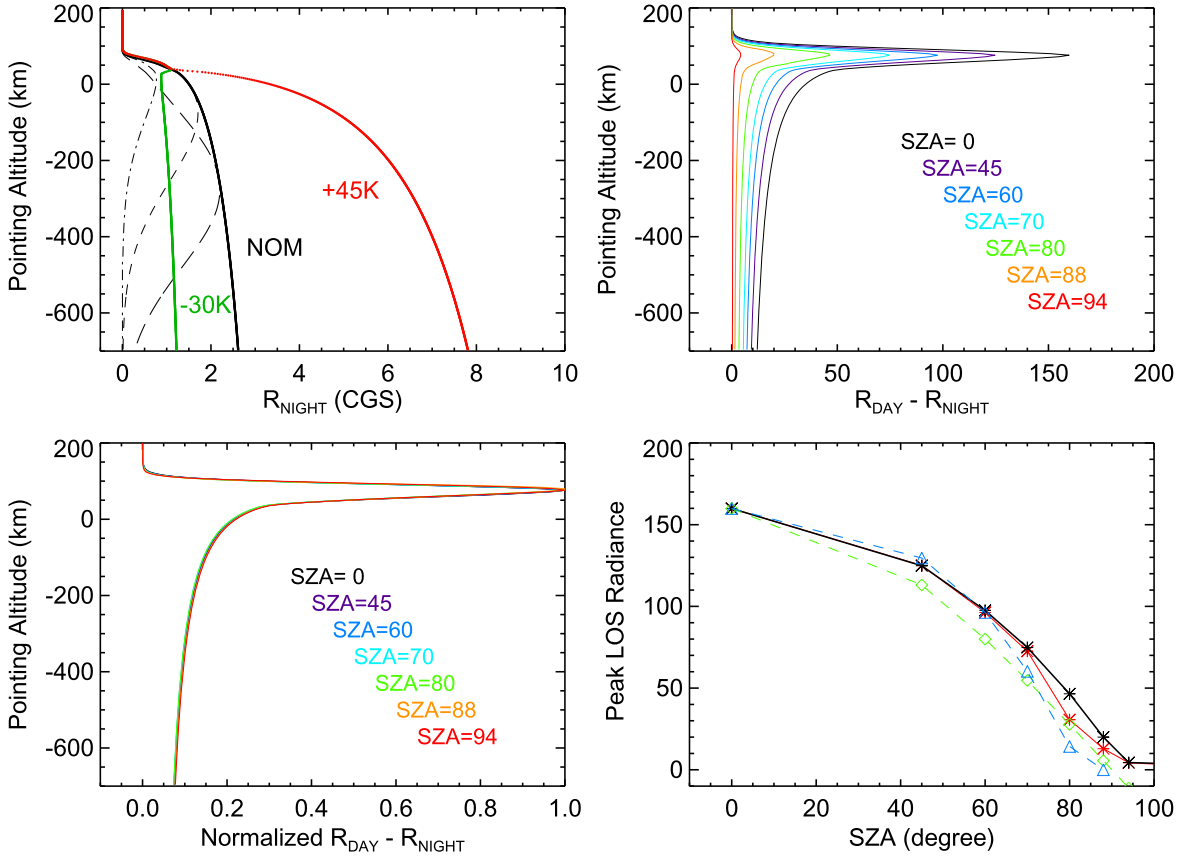

Figure 12. LTE vs. non-LTE simulations. (a) Calculations of $R_{\rm LOS}$ for the three tropospheric profiles in Figure 4. Dashed lines: nominal result after convolution with Airy functions pointing at the surface and at ±250 km. (b) Radiance profiles for diverse SZA after removing the LTE component. (c) Normalization of the profiles in panel (b) to their peak emission. (d) Variation of peak emission with SZA and fit with an exponential function (see text).

normalize the $R_{\rm LOS}^{\rm MESO}$ profiles to their peak mesospheric values in order to highlight this effect, we obtain a normalized mesospheric component, or $R_{N,{\rm LOS}}^{\rm MESO}$, with exactly the same profile for all SZAs, as shown in the bottom-left panel of Figure 12. This result illustrates a "universal functional" for the non-LTE mesospheric component that is used in the wind derivation, and is further analyzed in the next section.

Notice that the variation of the peak emission with SZA departs from a simple cosine law at high SZA values. This is shown in the bottom-right panel of Figure 12. This panel also shows the very similar variation with SZA of the vibrational population of the upper state of the transition, the $CO_2(001)$ state, at 80 km altitude (red line). This population density follows the dependence on SZA of the atmospheric transmission to space, $T_{\rm SPACE}$. This is an exponential of the "oblique optical depth," i.e., the ratio of the optical depths in the normal and in $\mu = \cos({\rm SZA})$: $T_{\rm SPACE} \approx \exp(-{\rm Opt.Depth}/\mu)$. At the peak layer, the optical depth in the normal is essentially the same for all SZA. To better illustrate this SZA dependence we added two fitting functions of μ in the figure: an exponential (blue line) and a cosine law (green line). It is well known that a more realistic oblique optical depth is obtained by replacing μ with a grazing function at high SZA. Otherwise both fits overestimate the oblique optical depth and give unrealistically low transmittances (and emissions) near SZA = 90°, as shown in the figure.

6. FORWARD MODEL PARAMETERIZATION AND UNCERTAINTIES

6.1. Parameterization of the Upper Atmospheric Contribution

Inspection of the shape of the LOS-integrated contribution functions after removing the nighttime (tropospheric) part and normalizing at the peak, or $R_{N,{\rm LOS}}^{\rm MESO}$, as shown in the right panel of Figure 12, reveals a "generic" function that is valid for all atmospheric conditions and SZA. We can recognize three regions, each one showing a distinct altitude variation, and all of them related to a few geophysical parameters. Their transition altitudes can be established around 45 and 100 km in the case of Mars, but variations of ±10 km in any of them do not alter the present discussion.

Region A. Mesospheric peak emission.

The location of the peak is related to the altitude of the maximum non-LTE excitation, although slightly lower due to geometrical considerations. Since the non-LTE excitation follows the solar absorption, it is well represented by a Chapman-like layer, i.e., a Gaussian around the peak. For Mars and the spectral line studied here it is centered around 75 km (the peak emission layer in our reference atmosphere) and its width is a few atmospheric scale heights. The peak altitude could be any approximate value for our purpose; its variations with latitude, season, or dust loading are not important here.

Region B. Thermospheric behavior.

Above the mesospheric peak, in very optically thin conditions, there is a density-driven exponential decrease of the radiative contributions, which can also be related to the scale height of the atmosphere.

Region C. Optically thick region.

At the other extreme of the function, in the lowest tangent paths of the limb portion of the beam and in the whole nadir portion, the emission varies with the emission angle associated with each LOS. These changes follow from the variable thickness of the non-LTE emission layer as projected along the LOS at each pointing altitude.

This generic non-LTE $R^{\rm MESO}_{N,\rm LOS}$ function can be approximated very well by the following three analytical expressions, one for each of the three regions:

$$\text{Region A:}\quad 45\,\text{km} < z \leqslant 100\,\text{km}$$
$$R^{\rm MESO}_{N,\rm LOS} = R^{\rm MESO}_{N,\rm LOS}(z_{\rm peak})\exp\left(-2X^2\right) \tag{4a}$$

$$\text{Region B:}\quad 100\,\text{km} < z$$
$$\ln R^{\rm MESO}_{N,\rm LOS} = \ln R^{\rm MESO}_{N,\rm LOS}(z_{100}) - (z - z_{100})/H \tag{4b}$$

$$\text{Region C:}\quad -700\,\text{km} < z \leqslant 45\,\text{km}$$
$$R^{\rm MESO}_{N,\rm LOS} = \sqrt{(R_\delta + z_{\rm peak} + \Delta z)^2 - (R_\delta + z)^2} - \sqrt{(R_\delta + z_{\rm peak})^2 - (R_\delta + z)^2} \tag{4c}$$

where the parameters used in these expressions are $z_{100} = 100\,\text{km}$ and $\ln R^{\rm MESO}_{N,\rm LOS}(z_{100}) = 0.27$; a typical scale height of $H = 10\,\text{km}$ can be used in the thermosphere; $X = (z - z_{\rm peak})/\Delta z$, $z_{\rm peak} = 75\,\text{km}$, $R^{\rm MESO}_{N,\rm LOS}(z_{\rm peak}) = 1$, $\Delta z = 32\,\text{km}$ and the planet's radius $R_\delta = 3390\,\text{km}$.

Some of these values, like the altitude of the emission peak or the width of the non-LTE region Δz, are specific to the spectral line used in this study. However, small variations in these parameters do not significantly affect the fit of $R^{\rm MESO}_{N,\rm LOS}(z)$, so this function can be used confidently for spectral lines of similar strengths in the 10 μm band.

The main advantage of an analytical expression for $R^{\rm MESO}_{N,\rm LOS}$ in terms of geophysical parameters is that one can adapt the functional fit to other FOV if necessary, therefore extending this method in principle to any beam size and observational campaign (an extension beyond the 700 km depth for example is straightforward).

6.2. Brief Practical Guide to Create Your Own Non-LTE Forward Model

An observer can use the result of the previous section, along with the steps given in Section 2, to build a forward model appropriate for a given campaign. Let us focus on Mars in this discussion.

First, the user should take the function $R^{\rm MESO}_{N,\rm LOS}$ from Equation (4) and scale it with the peak emission radiance at the correct SZA of the observations in order to obtain $R^{\rm MESO}_{\rm LOS}$. As the SZA variation does not obey a cosine law at high SZA, the values in Figure 12 (top-right panel) should be used. Spectral lines other than P4 of the 10 μm band require a correction factor (the ratio of the line strengths) at all altitudes in order to have a more realistic emission level. However, it is the shape of $R^{\rm MESO}_{\rm LOS}$ and its variation with SZA, rather than a precise emission level, that is relevant to the present discussion.

If the total radiance measured, rather than the mesospheric-only contribution, is of interest, then a second step would be to modify the "mesospheric" $R^{\rm MESO}_{\rm LOS}$ by adding a tropospheric contribution according to the actual thermal structure in order to generate a correct $R_{\rm LOS}$ profile. As mentioned above, since the tropospheric state is unknown and only a climatological estimate can be used, this step represents an uncertainty that can be significant at high SZA.

The next two steps correspond to steps 4 and 5 in Section 2. The resultant $R^{\rm MESO}_{\rm LOS}$ (or for radiance simulations, the $R_{\rm LOS}$ combining tropospheric and mesospheric values) needs to be further convolved with the beam/Airy function to generate the MaxInf region mapped by each observation. For a given short campaign the FOV and beam function may be common to all observations, but not necessarily so for different campaigns and different telescopes. And finally, a further convolution with a given climatology of Martian winds like the MCD (after a projection along the LOS to obtain $u_{\rm LOS}$) would allow an estimate of the model-expected wind and a comparison with the measured values.

6.3. Evaluation of Uncertainties

We discussed above various uncertainties related to the observation of winds at mesospheric altitudes on Mars and Venus that can be incorporated into uncertainties of the forward model. In turn, they will be converted into error bars of the measured winds using the results of our sensitivity study. Again, let us focus on Mars and use $\hat{u}$ for the averaged wind component to be observed, and simulated with our forward model F; then Equation (1) can be written as

$$\hat{u} = F\,(u_{\rm LOS},\,\text{SZA},\,T,\,\text{geometry},\,\text{non-LTE},...) + \epsilon_M$$

where $u_{\rm LOS}$ is the actual wind (along the LOS), ϵ_M is the measurement error (expressed in wind units), and non-LTE means all the non-LTE parameters. The error associated with $\hat{u}$ will have as many components as relevant variables of F. Considering a generic parameter p with an associated uncertainty δp_K, the error ϵ we are looking for will contain the following component:

$$\epsilon\,(p_K) = \frac{dF}{dp_K}\,\delta p_K.$$

Needless to say that the correct evaluation of the sensitivities dF/dp_K requires a precise and realistic forward model.

We carried out such an evaluation for all the uncertainty sources of the forward model identified in this study, and Table 1 shows how they contribute to the total error of the winds observed (or simulated). We have also added typical measurement uncertainties, for reference. The actual values are only valid for Mars; for brevity's sake, a similar exercise for Venus is omitted.

The table does not include minor effects mentioned above like the variation of the Doppler shift along the LOS or the asymmetry of the SZA within the beam. Some of the entries are difficult to estimate, like the atmospheric variations within the beam. They vary with integration time and beam size, in addition to the actual Mars location and season. Exploration of the MCD for the conditions of Campaign C of Sonnabend et al. (2012) gives small changes in the thermal structure and in the winds around the averaged state, and we expect this to be a general result.

Table 1
Error Components of the Forward Model and of the Observations

	Error Sources	Error[a]	Evaluation
Forward Model Errors	Beam pointing, ϵ_1	6%–10%[b]	Figure 9 (see text)
	Grid (z, x_{LOS}, α), ϵ_2	Small	Section 4
	Airy function, ϵ_3	4%[c]	Section 4
	Non-LTE, ϵ_4	Small	Section 5
	T in mesosphere, ϵ_5	Small	Section 5.1
	T in troposphere, ϵ_6	Small[d]	Sections 5.1 and 5.2
	Peak emission altitude, ϵ_7	<10 km	Section 5.1
	Local atmospheric variations, ϵ_8	Small Variable[e]	MCD
	Analytical fit to F, ϵ_9	<5% [f]	Section 6.1
	Assumed wind field, ϵ_{10}	Proportional[g]	Equation (3)
Measurement Errors	Spectral Resolution, ϵ_R	10 m s^{-1}	Sonnabend et al. (2012)
	Line fit, ϵ_F	<20 m s^{-1}	Sonnabend et al. (2012)
	Other instrumental, ϵ_I	8 m s^{-1}[h]	Sonnabend et al. (2012)

Notes.
[a] Means standard deviation of a random error. Expressed as absolute (m s^{-1}) or relative (%) wind speed.
[b] Values appropriate for SZA $\leqslant 60°$ and for an alignment error of $\sim 1/3$ FOV. If seeing conditions or unwanted telescopic motions are important, the fraction of FOV uncertainties and the total error will be larger. In addition, an equivalent horizontal uncertainty will represent a few extra degrees of averaging in latitude, the precise value depending on beam size.
[c] The Gaussian approximation to the Airy function varies a little with the beam size. In our case, 4% is appropriate for a "good" pointing (neither vertical nor latitudinal shifts).
[d] Varies a lot with SZA, and its uncertainty on the emerging radiance can be up to 100% (see Figures 10 and 12 and discussion in Section 5.1), but its impact on the winds is negligible.
[e] This refers to the natural atmospheric variability within the beam and during the integration time. An obvious resource to evaluate these is the Mars Climate Database (see text).
[f] The analytical fit gives integrated radiance errors of ~2% but we increased it to account for possible interpolation errors in our SZA grid (see Figure 12, top-right panel).
[g] This refers to the uncertainty in the wind speeds used within the forward model. The simulated wind and its errors are proportional to the winds assumed (after the weightings), so some caution is required when selecting these. Notice that this is a formal error, only required for comparison with model/climatological predictions.
[h] Other random instrumental errors like calibration issues, time-step of the Doppler shift calculation, etc.

Other entries, although in principle independent of the atmospheric state, are related to the previous point, like the beam uncertainty at high SZA. At higher SZA the importance of the nadir portion to the measured radiance is larger, as is the pointing uncertainty, but not to the winds obtained.

In the next section we will explore the important effect of the troposphere on the radiance measured, although the effect on the winds is very small. Other aspects like the seasonal variations and related uncertainties will be explored in more depth in a forthcoming publication.

The total error budget is the quadratic summation of all the variances $\epsilon^2 = \sum_k \epsilon_k^2$. From the results in Table 1, the most important uncertainty source in the forward model is the beam pointing. Table 1 also reveals that the forward model errors represent a small fraction of the total error, particularly for low wind speeds. The measurement and instrumental components give a wind-independent error source that dominates the error budget. These instrumental errors imply that measured wind speeds below about 13 m s^{-1} are smaller than their uncertainty.

As an example, let us consider the case of our idealized constant wind field of 85 m s^{-1} in the Martian mesosphere. As computed above, a hypothetical observation of such wind under a solar illumination of SZA = 60° would give a measured (averaged) value of 82 m s^{-1} (see Figure 8). What is the proper error bar for this value? Starting from the forward model, a conservative estimation should use the upper limit of each error component, for example $\epsilon_9 = 5\%$ and $\epsilon_1 = 10\%$, and assume a given minimum value for all the "small" terms $\epsilon_2 = \epsilon_4 = \epsilon_5 = \epsilon_8 \sim 1\%$. For ϵ_6 we will see below that a value around 7% could be appropriate for our SZA = 60° observation. The total uncertainty of the forward model therefore amounts to about 12%, or ± 10 m s^{-1}. To add typical measurement errors, let us look at a real example with a wind speed and SZA close to our hypothetical case, such as the determination around 60° N in Campaign C of Sonnabend et al. (2012), whose reported value is 85 m s^{-1} $\pm$ 21 m s^{-1}, i.e., a total measurement error close to 25%. The spectral resolution error $\epsilon_R = 10$ m s^{-1} can be transformed into a 12% error before it is combined with all the forward model errors. A similar transformation for $\epsilon_I = 8$ m s^{-1} gives 10%. An estimation for the remaining component is $\epsilon_F = 17$ m s^{-1}, or 20% (the three measurement errors combine to reproduce the reported 21 m s^{-1}). The composite error including measurement and forward model errors is now 27%. This is only a little above their reported error, because the measurement terms are large. Our hypothetical measurement could therefore be 82 m s^{-1} $\pm$ 22 m s^{-1}. This estimation can be considered as a first approximation valid for all wind determinations larger than the 13 m s^{-1} value mentioned above (smallest wind detectable with current instrumentation). In other words, our forward model errors amount to approximately 12% of the measured wind.

7. APPLICATIONS

7.1. Revisiting Previous Observations

We have applied the strategy in previous sections to the set of observations reported by Sonnabend et al. (2012), spanning about three Martian years, and revised their error budget. We

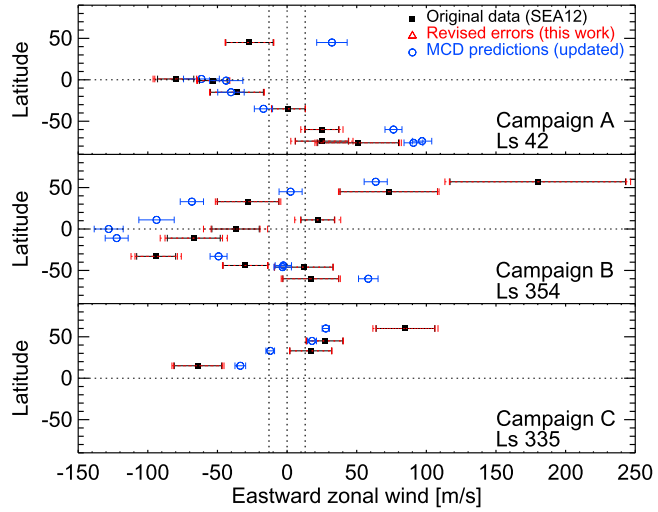

Figure 13. Revision of Figure 8 of Sonnabend et al. (2012) by adding forward model error components. Black: original values from Sonnabend et al. (2012). Red: our calculation, with two sizes of the error bars, one derived from the observed winds and the other from the MCD winds. Blue: MCD appropriate for the singular location and time of each observation; MCD uncertainties refer to those within the beam size and due to the integration time. Dashed vertical lines at -13 and $+13$ m s^{-1} indicate the region of caution due to winds smaller than typical instrumental uncertainties. See text.

evaluated an error component from our forward model uncertainty study (Table 1) and using both the wind speeds obtained by Sonnabend et al. (2012) and the winds extracted from the MCD v.4 at the 0.001 mbar level.

Figure 13 shows the results of this study applied to the three campaigns of Sonnabend et al. (2012). Note that the variability in the GCM winds is smaller than in Sonnabend et al. (2012) because we extracted the GCM winds at the precise time and location of the observation and our variability includes only the changes within the beam size and integration time. The changes in the data points are not large and the global conclusions have not changed from Sonnabend et al. (2012). Even when using the MCD winds in the error analysis in the cases where they are larger than the observed winds, the forward model errors have a small impact. There are several clear discrepancies between model and data, particularly at equatorial latitudes in Campaign B, with larger westward winds in the MCD. The comparison at high latitudes is not that clear. We encourage more observations in both of these latitude ranges and during both solstice and equinox conditions.

Although this is an improvement over the study of Sonnabend et al. (2012) it still lacks two features: a more detailed handling of MCD wind variability and a proper 3D projection of the extracted winds. This should be applied to each observation and it will be the topic of a future work, which might alter the present discussion for some of the data points.

7.2. Recommendations to Observers

Next we list and extend some recommendations for future observations, based on our results. We want to start by recalling that this work relies only on precise measurements of the core of the emission lines in the 10 μm band. We therefore urge observers to evaluate carefully the errors during the fitting of this parameter.

A basic recommendation is to observe the limb of Mars or Venus under strong solar illumination, since the atmospheric non-LTE emission will be larger, the beam pointing error smaller, and the integration time and signal-to-noise errors will also be smaller.

7.2.1. Optimize the Pointing

A second recommendation, based on the results of Figure 7, is to raise the pointing of the beam a little above the limb of the planet. This would have a double effect: first, to reduce the sensitivity of the Airy function at the radiative peak contribution, which will increase the integration time needed to get the same signal; and second, to reduce the nadir component. To determine how much to shift the beam from the planet's edge, we need a compromise between the following three aspects: (1) the benefit for the atmospheric limb, (2) the reduction of the Airy function away from the center of the beam, and (3) the risk of missing the planet during the observation.

A quantitative criterion for the first two points could be that the shift guarantees that the non-LTE emission region falls within the 50% response of the Airy function. Let us focus on Mars and call f_{50} the distance from the beam center where the Airy response falls to 50%, and let us express it in units of the beam radius $R_{\rm BEAM}$ (i.e., f_{50} is a fraction of $R_{\rm BEAM}$). If $R_{\rm BEAM}$ is expressed in km, as projected on the Martian disk, then a convenient shift in the pointing would be SHIFT $=$ $50 + f_{50} R_{\rm BEAM}$. The 50 km value is approximately the base of the strong non-LTE emission on Mars. However, let us consider now the telescopic pointing uncertainty (point (3) above). If this is expressed as a fraction $f_{\rm POINTING}$ of $R_{\rm BEAM}$, we can address this aspect by adding half its uncertainty to the SHIFT. Our final proposal is therefore SHIFT $=$ $50 + (f_{50} - 0.5 f_{\rm POINTING}) R_{\rm BEAM}$. Note that if the uncertainty in the pointing is large or comparable to the core region of the Airy function ($0.5 f_{\rm POINTING} > f_{50}$) then there is no advantage in shifting the telescope's beam.

7.2.2. Prioritize Nighttime Viewpoints for High SZA

The large effect of SZA on the $R_{\rm LOS}$ profile suggests a practical application in remote sensing. Such a variation could be used as an advantage for observations if a small portion of the planet's disk has a strong solar illumination and the rest is poorly lit. The limb contribution would be enhanced. As an example, it seems better to observe the mesosphere of Mars under an illumination of, let us say, SZA $= 60^\circ$ from the nightside than from the dayside. This is illustrated in Figure 14, where the portion of the Martian disk within the beam-projected disk has SZA larger than 60° in the nightside perspective, therefore giving a smaller contribution than in the dayside perspective.

Using the results for Mars shown in Figure 11 for the nominal thermal structure and beam size used in this work, we calculated that for SZA $= 60^\circ$ the limb contribution would go from 33% in the dayside view to 58% in the nightside view. This variation increases with SZA. For SZA $= 70^\circ$ the change in the limb contribution goes from 29% to 70% (from the dayside to the nightside view), and for SZA $= 50^\circ$ the change is more modest, from 33% to 47%. For SZA $\leqslant 40^\circ$ the effect is very small. This is illustrated in Figure 15. These values will differ for a different Martian thermal structure and for Venus but the argument is equally valid.

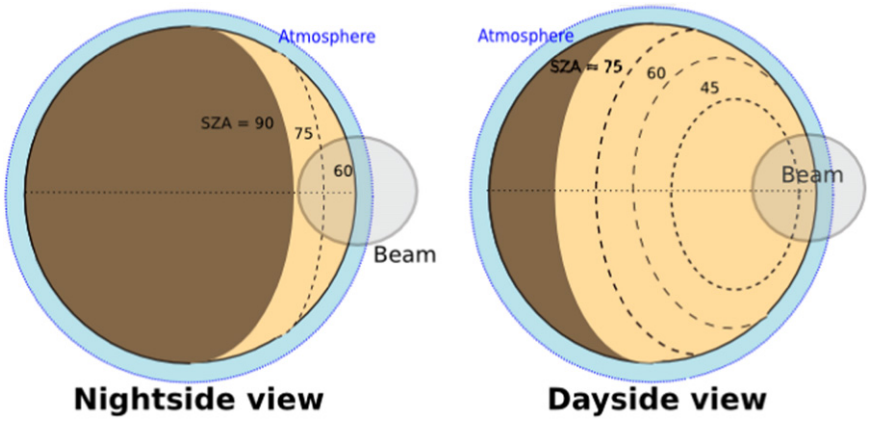

Figure 14. SZA variability within the beam-projected area on the Martian disk in two conditions, nightside (left) and dayside (right) views (perspective from Earth). In both cases the solar illumination on the limb is the same, SZA = 60°.

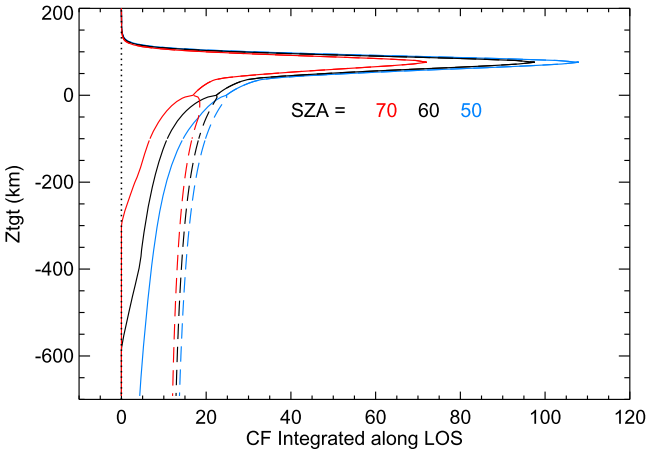

Figure 15. Impact of a dayside/nightside view for SZA = 50°, 60°, 70° at the tangent point. Dashed lines: dayside view. Solid lines: nightside view. See Figure 14 and text for details.

7.2.3. Improve Upon Previous Knowledge of Wind Speeds

Instrumental errors and noise represent an unavoidable source that is independent of the observed wind speed. This error component will be less relevant the larger the wind speed is. According to errors ϵ_R and ϵ_I in Table 1, which follow the work of Sonnabend et al. (2012) for Mars, wind speeds below about 13 m s^{-1} will be within instrumental noise. An obvious recommendation is therefore to observe the Mars mesosphere where the mesospheric winds are expected to be the largest. This is the case during equinox at low latitudes and during solstices at mid–high latitudes of the winter hemisphere (see for example Figure 2 in Sonnabend et al. 2012). However, in the latter case the SZA is very high, and therefore observing low to mid-latitudes might be a better choice. A similar argument applies to the Venusian winds around 110 km, although we lack data-validated information about where and when they are the largest.

One of the goals of this study is to permit meaningful comparisons with the Martian GCM predictions. These include wind magnitudes and variabilities. The variability of the predicted winds is also a piece of information to consider when planning future observations. Further recommendations along these lines, studying the atmospheric variability of the wind and temperature fields, as we know them from state-of-the-art Martian GCMs, will be addressed in a future work.

8. SUMMARY

We have studied how the geometry of the problem of observing the limb of Mars and Venus from ground-based telescopes requires a detailed handling of three functions whose convolution describes the observing system and the 10 μm measurements. Those functions follow the proper weightings, including limb and nadir ray-tracings, the projected winds along the LOS, and the Airy function of the telescope's beam cross section. We built a detailed forward model that included these functions and which, upon assuming a given wind field, was used to simulate the radiances and the winds derived from their Doppler shifts during typical observation conditions. The study of their convolution allowed us to estimate the importance of each of those functions, to quantify the uncertainties for typical measurements at 10 μm, and to suggest recommendations for future observations. Although we focused on Mars and performed a specific study for an idealized wind field and for a geometry taken from a given observation campaign, we tried to extract conclusions valid for all previous and future observations as well as for the case of Venus.

A major result of this work is that there are two radiance components mapped at 10 μm, one from the mesosphere and another from the troposphere (in the case of Venus: upper and lower mesosphere). This tropospheric emission is not in contradiction with the usual notion that the troposphere normally does produce an absorption of the surface emission in the far wings; we refer here to the tropospheric emission in the line's core. Simulations revealed a strong limb-brightening due to the non-LTE mesospheric emission, which also affects the nadir portion of the disk. If nighttime observations were performed, or if we selected the line's wing during daytime, there would be a limb-darkening due to the usual decrease in temperature at tropospheric altitudes. The tropospheric component is uncertain due to the variable thermal state of the Martian troposphere, although a quantitative estimation of this term is possible using climatological predictions.

However, only one of those components, the mesospheric non-LTE emission, matters for wind determinations. This is because only the line core emission is used during the fitting to derive the Doppler shift. Therefore the tropospheric winds and temperatures have a negligible impact on the mesospheric winds. The atmospheric altitudes producing the line emission

extend from 50 to 110 km on Mars, and 90 to 130 km on Venus, approximately.

The mesospheric component varies a lot with SZA and usually dominates at low SZA. A parameterization of this component with SZA and altitude was proposed in Section 6.1 for Mars. It makes use of only a few geophysical parameters, and we proposed that similar parameterizations can be applied to Venus and to other hypothetical CO_2 atmospheres.

We also performed a detailed analysis of the diverse forward model errors (Section 6.3), again with a focus on the Martian case. The dominant source of uncertainties in the winds is the beam pointing, followed by the Airy function. Still, these uncertainties are normally smaller than instrumental errors and noise.

We produced general guidelines for future observers based on our forward model calculations, which we recall here. First, we discussed how to build an appropriate forward model to describe the observations (Section 6.2). Second, we listed some precautions when designing observations and when comparing the measurements with models or databases like the MCD (Section 7.2). In particular, we proposed favoring observations with strong solar illumination. If the pointing accuracy permits it, a pointing centered a little outside the planet's edge can greatly reduce the nadir component. Also, observing the planet's limb from the "nightside" perspective can be advantageous at moderate to high SZA. Previous information on winds and the thermal structure can be used to plan observations when the mesospheric winds are particularly strong.

Finally, we applied this method to revise the error analyis of a set of observations extended over several Martian years in Section 7.1. For such a purpose we extracted the likely mesospheric winds from the MCD at the precise location and timing of the observations. Corrections were made to the error bars by including our forward model errors, and most of the observations increased their error bars by small amounts. We confirm the general agreement obtained by Sonnabend et al. (2012) between their data and the MCD. In spite of this general agreement, there seems to be a clear discrepancy at low latitudes in Campaign B, with larger westward winds in the MCD than in the data. Incidentally, we used the MCD version v.4 in our plots, which should be revisited in the light of new versions. More observations at equatorial and high latitudes would be desirable. A detailed study of the impact of variabilities of the predicted wind, including 3D projection on the comparison, is an ongoing work and will be presented elsewhere.

We hope this work encourages observers to continue to optimize campaigns of ground-based observations of the mesospheres of Mars and Venus, and modelers to pay attention and validate their results at those altitudes against these valuable data sets.

M.A.L.-V. was supported by the Spanish MINECO through the CONSOLIDER program ASTROMOL CSD2009-00038 and through the Spanish National Plan project AYA2011-30613-CO2-1. M.A.L.-V. also acknowledges support through the ESA project 4000106548/12/NL/AF devoted to maintenance of the Mars Climate Database and through the project UPWARDS-633127 under the European Union's Horizon 2020 Programme (H2020-Compet-08-2014). L.M. acknowledges support by the German Research Foundation (DFG), Grant to Support the Initiation of International Collaboration SO 879/2-1.

APPENDIX
RADIATIVE CONTRIBUTION FUNCTION AND OTHER DEFINITIONS

To clarify the definition of "radiative contribution function," C, and the difference from the more common term "radiative weighting function," let us consider a particular LOS in Figure 2 that points to a tangent altitude z and is discretized into a number of path segments.

The "contribution function" of a given segment, at position $x_{\rm LOS}$ along the LOS, is the part of the emerging radiance $R_{\rm LOS}(z)$ that comes from that segment. The integral along the LOS of all the contribution functions is the emerging radiance $R_{\rm LOS}$:

$$R_{\rm LOS}(z) = \int_{x_{\rm LOS}} C(z, x_{\rm LOS}) dx_{\rm LOS}. \quad (5)$$

According to the formal solution of the radiative transfer equation, the C term is

$$C(z, x_{\rm LOS}) = J(x_{\rm LOS}) \frac{d\mathcal{T}(x_{\rm LOS}, \infty)}{d\ x_{\rm LOS}}$$

where $J(x_{\rm LOS})$ is the non-LTE source function at $x_{\rm LOS}$ (or the blackbody at the local temperature if in LTE) and $\mathcal{T}(x_{\rm LOS}, \infty)$ is the atmospheric transmittance from there to space along the LOS. The derivative of this transmittance is normally called the "weighting function" and describes how the opacity varies across the layer, regardless of the emission of the layer itself. Therefore the contribution function is the product of the weighting function and the source function. It incorporates the emission properties in the layer, and evaluates the actual emission from that layer that reaches space. The units of C in the cgs system are erg s^{-1} cm^{-3} sr^{-1} cm^{-1} when radiance is expressed in erg s^{-1} cm^{-2} sr^{-1} cm^{-1}.

The calculation of C therefore requires the calculation of non-LTE source functions and line-by-line transmittances at high spectral resolution. These are performed with our Martian non-LTE model (Lopez-Valverde & Lopez-Puertas 1994; López-Valverde et al. 2011) and with the RFM line-by-line code (Dudhia 2000). The calculation also requires a discretization of the above equation. As explained in Section 3 we used 4 km steps in z and 10 km steps in $x_{\rm LOS}$. The non-LTE source function can be expressed in terms of the number population of the excited state (001), which is the magnitude shown in Figure 4, or in terms of vibrational temperatures, as used in other works (López-Valverde et al. 2011).

Another useful concept used in Section 3, from López-Valverde et al. (2011), is the radiance $R^{\rm OBS}$ detected by an observer located at a given point $x_{\rm OBS}$ along the LOS:

$$R_{\rm OBS}(x_{\rm OBS}) = \int_{-\infty}^{x_{\rm OBS}} J(x_{\rm LOS}) \frac{d\mathcal{T}(x_{\rm LOS}, x_{\rm OBS})}{d\ x_{\rm LOS}} dx_{\rm LOS}.$$

Figure 5 shows how this function varies along the LOS and its relation to C.

We can see two special cases:

Table 2
List of Mathematical Symbols and Definitions

Symbol	Definition
u or $\hat{u}$	Modulus of the wind field in Mars' atmosphere (measured or simulated, respectively)
z	Pointing altitude above the edge of Mars' solid body (see Figure 2)
$x_{\rm LOS}$	Distance along the LOS, with origin at the limb (see Figure 2)
α	Angle to describe the 2D cross section of the beam, zero at beam's center
LOS(z, α)	Line of sight, each of the individual ray pencils of the beam
$u_{\rm LOS}(z, x_{\rm LOS}, \alpha)$	Component of u along the line of sight at each point of the 3D beam
$A(z, \alpha)$	2D Airy function of the beam
$C(z, x_{\rm LOS}, \alpha)$	Radiative contribution function at each point of the 3D beam (see the Appendix)
$R_{\rm MEAS}$ or $\hat{R}$	Radiance measured from ground (see the Appendix), or simulated.
$R_{\rm LOS}(z, \alpha)$	Emerging radiance of a given LOS; $R_{\rm LOS}$ is used when α is either zero or irrelevant
$R_{\rm LOS}^{\rm MESO}$	Fraction of $R_{\rm LOS}$ due to the non-LTE mesospheric contribution only
$R_{N,{\rm LOS}}^{\rm MESO}$	Normalization of $R_{\rm LOS}^{\rm MESO}$ to its peak or largest value
$R_{\rm OBS}$	Radiance seen by an observer moving along the LOS away from Earth and looking at Mars (looking toward the left in Figure 3)
$R_{\rm OBS}^{\rm MESO}$	Fraction of $R_{\rm OBS}$ due to the non-LTE mesospheric contribution only.

1. If the point $x_{\rm OBS}$ moves toward Earth when it reaches the top of the atmosphere $x_{\rm OBS} = \infty$ and $R_{\rm OBS}(\infty) = R_{\rm LOS}$.
2. If we consider only the mesospheric component (integration along the LOS only for altitudes above about 50 km) then we can talk about an emerging "mesospheric radiance" for every pointing altitude "z":

$$R_{\rm LOS}^{\rm MESO}(z) = \int_{x_{\rm LOS}}^{\rm MESO} C(z, x_{\rm LOS}) dx_{\rm LOS}$$

and about a mesospheric emission seen by a moving observer along the LOS:

$$R_{\rm OBS}^{\rm MESO}(x_{\rm OBS}) = \int_{\rm MESO}^{x_{\rm OBS}} R_{\rm LOS}^{\rm MESO}(z) dx_{\rm LOS}.$$

Returning to Equation (5), integration over the whole beam gives the total radiance emitted by the atmosphere within the beam: $R_{\rm BEAM} = \int_z R_{\rm LOS}(z) dz$. If this includes the Airy function it results in the total radiance measured:

$$R_{\rm MEAS} = \int_z \int_\alpha R_{\rm LOS}(z) \times A(z, \alpha)\, d\alpha dz$$

which is the term $\hat{R}$ in (2). And if we focus on the mesospheric component only, we can equally define the mesospheric emission within the beam $R_{\rm BEAM} = \int_z R_{\rm LOS}^{\rm MESO}(z) dz$ and the total mesospheric radiance:

$$R_{\rm MEAS}^{\rm MESO} = \int_z \int_\alpha R_{\rm LOS}^{\rm MESO}(z) \times A(z, \alpha)\, d\alpha dz$$

which is the normalization term used in Equation (3) in Section 2.

Using this expression, the simulated mesospheric winds (Equation (3)) can be simplified, if we further assume that the wind is constant within the mesosphere, to

$$\begin{aligned} \hat{u} &= \frac{\int_z u_{\rm LOS}(z) \int_{x_{\rm LOS}}^{\rm MESO} C(z, x_{\rm LOS}) dx_{\rm LOS} dz}{\int_z \int_{x_{\rm LOS}}^{\rm MESO} C(z, x_{\rm LOS}) dx_{\rm LOS} dz} \\ &= \frac{\int_z u_{\rm LOS}(z) R_{\rm LOS}^{\rm MESO}(z) dz}{\int_z R_{\rm LOS}^{\rm MESO}(z) dz} \\ &= \frac{1}{R_{\rm MEAS}^{\rm MESO}} \int_z u_{\rm LOS}(z) R_{\rm LOS}^{\rm MESO}(z) dz \end{aligned} \quad (6)$$

where for simplicity we ignored the Airy-disk function. The averaged wind $\hat{u}$ is a composite of the mesospheric winds in each LOS weighted with their $R_{\rm LOS}^{\rm MESO}(z)$.

All the definitions used in this work are listed in Table 2.

REFERENCES

Betz, A. L., Johnson, M. A., McLaren, R. A., & Sutton, E. C. 1976, ApJL, 208, L141
Deming, D., & Mumma, M. J. 1983, Icar, 55, 356
Dudhia, A. 2000, Michelson Interferometer for Passive Atmospheric Sounding (MIPAS) Reference Forward Model (RFM) Software User's Manual (Oxford: Oxford Univ. Press)
Gilli, G., Lpez-Valverde, M., Peralta, J., et al. 2015, Icar, 248, 478
González-Galindo, F., Chaufray, J. Y., Lopez-Valderde, M. A., et al. 2013, JGR, 118, 2105
González-Galindo, F., Forget, F., López-Valverde, M. A., & Angelats i Coll, M. 2009, JGRE, 114, 8004
González-Galindo, F., Määttänen, A., Forget, F., & Spiga, A. 2011, Icar, 216, 10
Hedin, A. E., Niemann, H. B., Kasprzak, W. T., & Seiff, A. 1983, JGR, 88, 73
Johnson, M. A., Betz, A. L., McLaren, R. A., Townes, C. H., & Sutton, E. C. 1976, ApJL, 208, L145
Lebonnois, S., Forget, F., & Hourdin, F. 2008, AGU Fall Meeting, Abstract #U34B-02
Lellouch, E., Paubert, G., Moreno, R., & Moullet, A. 2008, P&SS, 56, 1355

Lopez-Valverde, M. A., & Lopez-Puertas, M. 1994, JGR, 99, 13117
López-Valverde, M. A., Sonnabend, G., Sornig, M., & Kroetz, P. 2011, P&SS, 59, 999
Millour, E., Forget, F., Spiga, A., et al. 2011, in Mars Atmosphere: Modelling and Observation, ed. F. Forget, & E. Millour (Paris: Laboratoire de Meteorologie Dynamique), 268
Mumma, M. J., Buhl, D., Chin, G., et al. 1981, Sci, 212, 45
Piccialli, A., Drossart, P., Lopez-Valverde, M. A., et al. 2011, in EPSC-DPS Joint Meeting 2011, 1837
Rodgers, C. D. 2000, in Inverse Methods for Atmospheric Sounding: Theory and Practice, Vol. 2, ed. F. W. Taylor (Singapore: World Scientific)
Roldán, C., López-Valverde, M. A., López-Puertas, M., & Edwards, D. P. 2000, Icar, 147, 11
Seiff, A., Schofield, J. T., Kliore, A. J., Taylor, F. W., & Limaye, S. S. 1985, AdSpR, 5, 3
Sonnabend, G., Sornig, M., Kroetz, P., & Stupar, D. 2012, Icar, 217, 315
Sonnabend, G., Sornig, M., Krötz, P. J., Schieder, R. T., & Fast, K. E. 2006, GeoRL, 33, 18201